Microrobot Design Using Fiber Reinforced Composites

R.J. Wood
School of Engineering & Applied Sciences
Harvard University
Cambridge, MA 02138
`rjwood@eecs.harvard.edu`

S. Avadhanula, R. Sahai, E. Steltz, R.S. Fearing[1]
Dept. of Electrical Engineering & Computer Sciences
University of California
Berkeley, California 94720
[1]`ronf@eecs.berkeley.edu`

Abstract— **Mobile microrobots with characteristic dimensions on the order of 1cm are difficult to design using either MEMS (microelectromechanical systems) technology or precision machining. This is due to the challenges associated with constructing the high strength links and high-speed, low-loss joints with micron scale features required for such systems. Here we present an entirely new framework for creating microrobots which makes novel use of composite materials. This framework includes a new fabrication process termed Smart Composite Microstructures (SCM) for integrating rigid links and large angle flexure joints through a laser micromachining and lamination process. We also present solutions to actuation and integrated wiring issues at this scale using SCM. Along with simple design rules that are customized for this process, our new complete microrobotic framework is a cheaper, quicker, and altogether superior method for creating microrobots that we hope will become the paradigm for robots at this scale.**

I. INTRODUCTION

All apparatus available for larger scale mechanical systems (motors, revolute joints, bearings, telescopic joints, and robust structural members) become more challenging as size decreases since surface effects begin to dominate over Newtonian forces [1]. For this reason, millimeter scale systems based on traditional 'macro'-scale manufacturing techniques are morphologically limited and articulated structures using revolute or sliding surfaces would be inefficient. Some preliminary MEMS structures have been attempted for microrobotic mechanisms such as hinge joints [2] and folded structures [3], microrobotic linkages [4], and prototype MEMS microrobots [5], [6]. These devices are constrained by the materials available and MEMS process limitations. Neither end of the manufacturing spectrum offers an acceptable solution for the creation of robust micromechanical systems which can be rapidly prototyped. Further, a holistic fabrication solution is desired; not a concatenation of numerous discrete technologies.

We have created a paradigm that incorporates all the mechanical and electromechanical devices that are required for the creation of complete, high performance microrobotic structures. This is something that has not been addressed or attempted elsewhere (either at this scale or with this complexity). Coupled with appropriate mechanical design, this paradigm for creating high performance microstructures is both enabling and holds the potential to eliminate the need for complex control and costly processes. This is based on flexure-jointed (compliant) mechanisms whose links and joints are fabricated in an integrated manner employing a laminate technology that uses high strength composite materials and polymers. This so-called Smart Composite Microstructures (SCM) technology is described in detail in a later section.

SCM is a solution to the shortcomings of MEMS and the limitations of macro-mechanical machining techniques. This was first introduced in [7] and expanded to include actuator systems in [8], [9]. The resulting structures are truly 3D, unlike the limited $2\frac{1}{2}$D devices that MEMS processes can create. Not only is this process more versatile than MEMS, it does not require cost-prohibitive infrastructure to implement and the entire process can be performed in a matter of hours (as opposed to months of significant manual

labor required for IC processes). Thus the paradigm that we present is an enabling technology for complete integrated microrobots and is simultaneously accessible due to its conceptual simplicity and low infrastructural cost.

In this work the SCM fabrication process is detailed for passive and active structures and a model is presented to describe the mechanics of these systems. The focus of the paper is on the production of the complete prototype in an integrated manner, and it provides the necessary procedures for the construction of rigid structural members, links and joints, actuators, electronics and sensors, and wiring. Note that SCM is presented as a *fabrication* process, not a *design flow* process. To address microsystem design, this paper also presents simple guidelines for preliminary design of prototype microrobots. These design rules are based on the mechanics of isotropic materials, but we also discuss laminate plate theory as a basis for describing SCM structures. Finally, examples are presented as verification of the SCM process.

II. SMART COMPOSITE MICROSTRUCTURE FABRICATION

The SCM fabrication process consists of laser micromachining constituent laminae to achieve a desired compliance profile by choice of geometry and material properties. Laser-cutting composite materials is not new, but when used to produce thin sheets with micron-scale features for millimeter-scale articulated laminates and actuators, this is a novel fabrication process. For the case of microrobotic structures, links and joints are created when polymers are sandwiched between face sheets of rigid composite materials where gaps in the face sheets create flexures. Actuators are made when any of the laminae are electroactive. Patterned conductive layers bring drive signals to the electroactive elements and allow sensors to be incorporated into the resulting structures. The design and construction of each of these elements is described here as one simple all-inclusive process.

A. Composite Process Details

Creating a simple flexure joint at this scale presents formidable challenges. Since the resulting static and dynamic parameters rely heavily on geometry, tolerances and alignment are crucial. Also, the creation of rigid links and compliant joints using the morphology shown in Fig. 3 requires either large aspect ratio machining and/or incorporating materials with different elastic properties. Flexure profile geometry along with an overview of the solution to creating rigid links and compliant joints is shown in Fig. 1. This solution uses both high aspect ratio, high precision machining, high modulus composite materials (e.g. carbon fiber or S-glass reinforced plastics), and robust thin film polymers.

To achieve the structures shown in Fig. 1, a 40μm thick sheet of unidirectional carbon fiber[1] prepreg (Fig. 1(1)) is micromachined by a pulsed laser[2] (Fig. 1(2)). The polymer layer is likewise machined using this laser. The choice of polymer was based upon compatibility

---

[1]M60J from Toray Carbon Fibers America, Inc.
[2]either a frequency doubled Nd:Yag laser ($\lambda = 532$nm, New Wave Research) or a UV excimer laser ($\lambda = 193$nm, TeoSys Engineering)
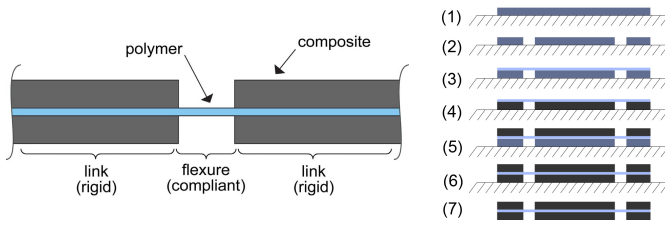
Fig. 1.   Rotational flexure mechanism and associated process.

Fig. 3.   Flexure diagram with geometric definitions.

with the matrix resin in the carbon fiber[3]. The cure cycle reaches a maximum temperature of $177°C$ using a curing profile of 4 hours. Therefore, a polymer layer capable of surviving this temperature, without embrittlement, is required. Polyimide film[4] has a sufficiently high service temperature (up to $400°C$) to survive the curing step.

Once cut, the polymer layer is aligned on the machined carbon fiber layer (Fig. 1(3)). Due to the inert nature of polyimide, simple weights or clamps to put pressure on the two layers while curing is not sufficient to ensure adhesion. We thus use a vacuum bagging process; vacuum film[5] is used in combination with a custom machined aluminum plate to hold the vacuum during curing. Concurrently, a perforated Teflon sheet and a breather cloth are used to prevent the resin's out-gassed bubbles from relieving pressure locally. This sufficiently places a uniform pressure on all areas of the sample. Autoclaving the assembly to apply greater pressure (drawing a vacuum over the sample and then pressurizing the oven) is also possible, however acceptable delamination resistance is observed with just one atmosphere of pressure.

Once cured (Fig. 1(4)), the polymer/carbon fiber is released and aligned onto another carbon fiber layer and cured using the same cycle again (Fig. 1(5)), producing the desired part (Fig. 1(6)). Example cuts and resulting flexures are shown in Fig. 2.
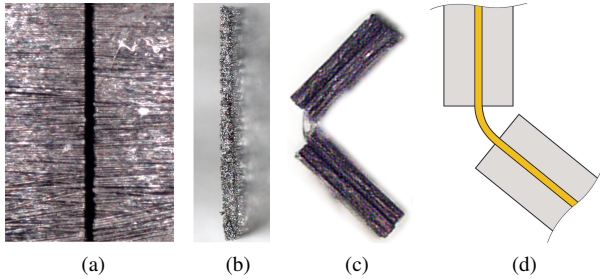

Fig. 2.   Laser cut detail (a) and cut fiber cross section (b). The cut width is approximately $10\mu m$ which is on the order of the fiber diameter. A folded flexure is shown in (c) along with a diagram of the flexure motion (d).

III. FLEXURE DESIGN

Traditional kinematic analysis assumes joints with perfect rotations about a desired axis. Since low friction pin joints are not possible at this scale, it is necessary to focus on the physical instantiation of the joints. When designing structures with flexures, it is necessary to ensure that the mechanical integrity of the flexures will not be compromised during use. The methodology for the design of simple beam flexures is presented in detail in [10], [11]; some of the pertinent ideas as they apply to the present case are repeated here for the sake of completeness. It should be noted that the materials that are considered for the flexures are amorphous polymers and are thus elastically isotropic (unlike what will be discussed for the link design).

[3]RS-3C from YLA Inc.
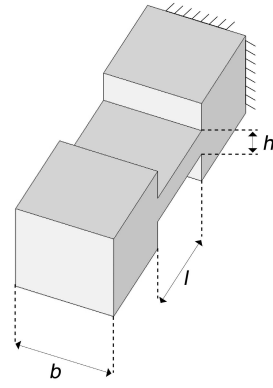[4]Kapton from DuPont
[5]Stretchlon 800 from Airtech

The rotational stiffness of the flexure may be estimated from elementary beam theory as EI/l, where E is the Young's modulus, I is the second moment of area, and l is the flexure length (see Fig. 3). It is noteworthy that the above relationship is accurate, even for large angular deflections, if the flexure is subjected to only pure bending. The model is less accurate if transverse and axial loads are also present. It is important to note the orientation of the flexures with respect to axial and transverse loads. This was described in detail in [12], but it will be noted here that the critical loading for axial buckling is typically much greater than the critical loading for transverse buckling.

In general, the flexure stiffness should be as small as possible. The stiffness can be reduced by decreasing E and I (since I is proportional to h^3, an effective way to reduce I is to reduce the flexure thickness) or by increasing the length l. The latter option is not desirable since axial flexure buckling strength is proportional to $1/l^2$.

A. Calculation of parallel stiffness

The parallel stiffness of a flexural mechanism is easy to calculate if we assume that each flexure is an ideal rotational joint with a constant rotational stiffness (similar to the pseudo-rigid-body model in [10]). In an N-link mechanism, the total potential energy (PE) stored in the flexures of the mechanism is given by:

$$PE_{tot} = \sum_{i=1}^{N} \frac{1}{2} k_i \gamma_i^2 \qquad (1)$$

where k_i is the stiffness of the ith flexure ($k_i = E_i I_i / l_i$) and γ_i is the total angular deflection of the ith flexure. To find the rotational stiffness of a single input mechanism with respect to the driving actuation angle, α, we need to first find the restoring moment for a given value of α. This is given by the gradient of the PE as:

$$
\begin{aligned}
M &= \frac{\partial PE}{\partial \alpha} \\
&= \sum_{i=1}^{N} k_i \gamma_i \frac{\partial \gamma_i}{\partial \alpha}
\end{aligned} \qquad (2)
$$

For small displacements about some nominal value of $\alpha = \alpha_0$, the stiffness of the mechanism is given as:

$$
\begin{aligned}
k_{eq} &= \left. \frac{\partial M}{\partial \alpha} \right|_{\alpha=\alpha_0} \\
&= \sum_{i=1}^{N} \left[k_i \left(\frac{\partial \gamma_i}{\partial \alpha} \right)^2 + k_i \gamma_i \frac{\partial^2 \gamma_i}{\partial \alpha^2} \right]
\end{aligned} \qquad (3)
$$

Due to the large change in stiffness with angle for some structures, this expression for k_{eq} is only valid for small motions. For the complete non-linear dynamics, we should directly use the value of the restoring moment M according to (2).

B. Flexure limits

The quantities that should be considered when designing simple beam flexures include the axial stiffness (Ebh/l), the revolute stiffness ($Ebh^3/12l$), and the ratio of axial to revolute stiffness ($12/h^2$). Ideally, the last quantity should be as large as possible. The maximum rotation that a conventional flexure can go through before yielding is also an important parameter and is given by:

$$\theta_{max} = \frac{2l\sigma_y}{Eh} \quad (4)$$

This last relationship can be easily derived from the formula for maximum bending stresses in a beam subjected to pure bending. Here σ_y represents the yield stress of the flexure material. As an example, for a $100\mu m$ long polyimide flexure[6], $\theta_{max} \approx \pm 40°$. As stated earlier, an important additional consideration in flexure design is the buckling of the flexure due to axial loads. Modeling the flexure as a link that is fixed at one end and free on the other, the critical load as determined from the standard Euler buckling relationship is given by:

$$P_{crit} = \frac{\pi^2 EI}{4l^2} \quad (5)$$

There can be problems associated with flexure mechanisms that don't occur with rotary joints such as undesired off-axis compliance and a non-stationary axis of rotation. These issues have been addressed with novel mechanisms such as split-tube flexures [11], redundant parallel compliant members [13], [14], and isolation and inversion mechanisms [15], and some of these concepts are appropriate for use with the SCM process. Off-axis compliance is a major concern since any undesired compliances within a serial transmission chain (for example, a desired rotation that is instead a combination of a rotation and flexure buckling) can exacerbate nonlinearities and backlash. Also, axis drift, if sufficiently severe can lead to undesired kinematic singularities or over-constrained parallel mechanisms.

One solution to undesired off-axis compliance is to avoid buckling by ensuring that some parts of a compliant mechanism are in tension at all times. Todd et al describe two ways to withstand high compressive loading in a compliant mechanism: isolation and inversion [15]. Prior to this, Wood introduced a flexure mechanism that was impervious to bucking under either compressive or tensile loading [7]. This device (shown in Fig. 4(a)) will have some flexural element in tension regardless of the polarity of the applied load (for small angular deflection). This is an ideal choice for high loading, low displacement applications and is enabled by the SCM process at the sub-millimeter scale.

For larger rotations, a different architecture known as a cross flexure minimizes off-axis motion by ensuring that some flexures are taut for rotations (shown in Fig. 4(b)).

C. Effect of flexure pre-stress

Note that in (3), γ_i represents the *total* displacement of the flexure from its strain-free state. This displacement depends not just on the kinematics of the mechanism but also on the fabrication method, which might impart a pre-stress to some of the flexures without any driving actuation. In other words, γ_i in (3) can be thought of as:

$$\gamma_i = \gamma_i^{kin} + \gamma_i^{fab} \quad (6)$$
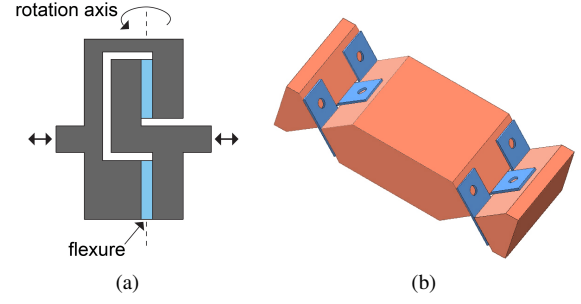
[6]Kapton 30HN from DuPont, $h = 7.6\mu m$

Fig. 4. No-buckling flexure (a) and cross flexures (b).

Here, $\gamma_i^{kin} = 0$ when the driving angle $\alpha = 0$ and γ_i^{fab} is the pre-stress in the joint which results from folding during assembly. Note that γ_i^{fab} is a constant for a given fabricated part. Since:

$$\frac{\partial \gamma_i}{\partial \alpha} = \frac{\gamma_i^{kin}}{\partial \alpha},$$

the first term in (3) depends purely on the kinematics and not on the initial pre-stress due to fabrication. Thus, we need to take the initial pre-stress of the flexure into consideration only for those flexures for which we have

$$\frac{\partial^2 \gamma_i}{\partial \alpha^2} \neq 0,$$

about the nominal operating point.

We can see the effect of pre-stressing on the stiffness of an example parallel mechanism (the spherical five-bar differential shown in Fig. 5(a)) in Fig. 5(b). There is almost a 100% increase in the differential stiffness when the θ_y flexure is pre-stressed by 90°. To minimize the effect of flexure pre-stress, it is useful to anneal the whole mechanism above the glass transition temperature, T_g, of the flexure material after the fabrication is complete (so long as this elevated temperature does not damage other sensitive structures). This has been demonstrated with polyester flexures ($T_g \approx 75°C$), but has not yet been attempted for polyimide flexures ($T_g \approx 400°C$).
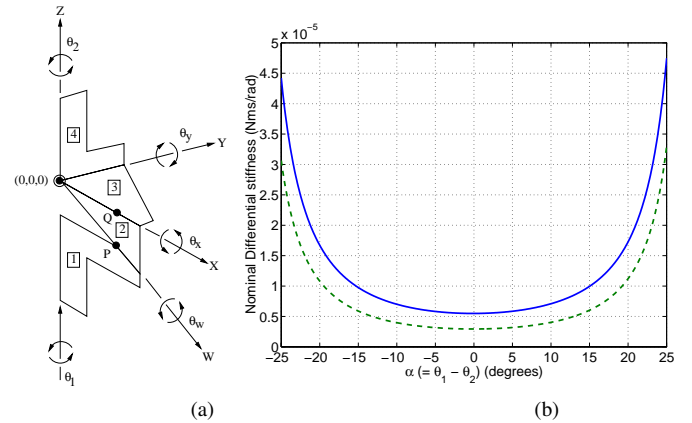

Fig. 5. Example of a spherical five-bar structure (a) in which certain joints are bent to 90° in the final assembly stage. The effect of this pre-stress is shown in (b). The solid line represents the stiffness of the differential w.r.t α when $\theta_y^0 = 90°$ and the dotted line represents the stiffness with $\theta_y^0 = 0°$.

D. Flexure alignment

The previous discussion described the effect of initial flexure position on the compliance of a series or parallel chain, i.e. how

improper configuration can increase the stiffness. Now we discuss the inverse: how poor choice of flexure orientation can lead to undesired compliance. Consider two basic singular four-bar mechanisms shown in Fig. 6(a&b). If the flexures were ideal pin joints, then in both cases the force F would not cause any motion (i.e. the two configurations would be infinitely stiff). If we perform a small motion FEA analysis on the two configurations, we find that the stiffness in the first case is almost an order of magnitude greater than the second. This result implies that it is advantageous to have the flexures oriented in such a manner that the force transmitted through them is always aligned along the axial length of the flexure.
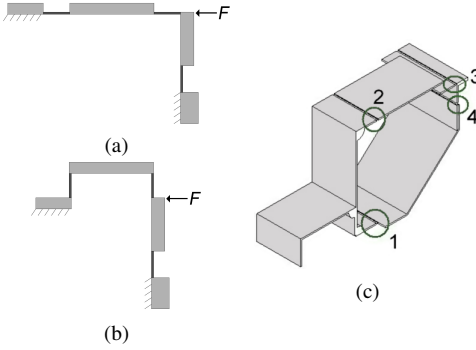

Fig. 6.   Singular four-bars for FEA analysis (a) & (b). The results from FEA show that when designing a flexure-based transmission system, it is advantageous to align the flexures with the expected loads. Using this simple design rule, a four-bar is shown in (c) in which the four axes (1-4) are aligned along the expected principal loading directions.

a) Effect of misalignment: Detailed analysis turns out to be extremely important in mechanisms where certain geometric constraints need to be met for the mechanism to move. Consider the differential mechanism shown in Fig. 5(a). It consists of two links labeled $\boxed{1}$ and $\boxed{4}$ which are actuated independently via two rotations. They are connected together by a series of three links which are interconnected by simple flexural elements. The basic idea is that when links $\boxed{1}$ and $\boxed{4}$ are moved in phase, the middle plate $\boxed{2}$ rotates along with them about their common axis Z. However, when $\boxed{1}$ and $\boxed{4}$ move out of phase, link $\boxed{2}$ also rotates about the other axes X, Y and W. The differential kinematics depends critically on the axes θ_x, θ_y, θ_z and θ_w shown in Fig. 5(a) intersecting at a single point. To ensure the kind of alignments we need, the laser-micromachining step of the SCM process cuts the entire differential mechanism as one piece (see Fig. 7(a)). It is important to note that alignment is so critical that we needed to account for the laser spot size. For structures in which alignment of adjacent pieces is this crucial, features are added to the design which mate and thus facilitate proper alignment (highlighted in Fig. 7(a)). By careful design, we have shown that we can reduce the parallel stiffness of a differential mechanism to just 1.5-1.6 times the predicted stiffness. This is quite a gain from previous designs which were almost 40-50 times the predicted stiffness.

IV. LINK DESIGN

Just as with the flexures, the link parameters are a function of the material geometry and in this case the elastic anisotropy and lamina orientations as well. For kinematic analysis to be valid, a reasonable requirement is that the link stiffnesses are much greater than the flexure stiffnesses so that none of link stiffness terms need to be included in the calculation of the total potential energy in (1). This can be be formalized in the following way,

$$\min_n k_n^{\text{link}} = \min_n \frac{b_n \left[D_{11}\right]_n}{l_n} >> \max_i k_i \tag{7}$$
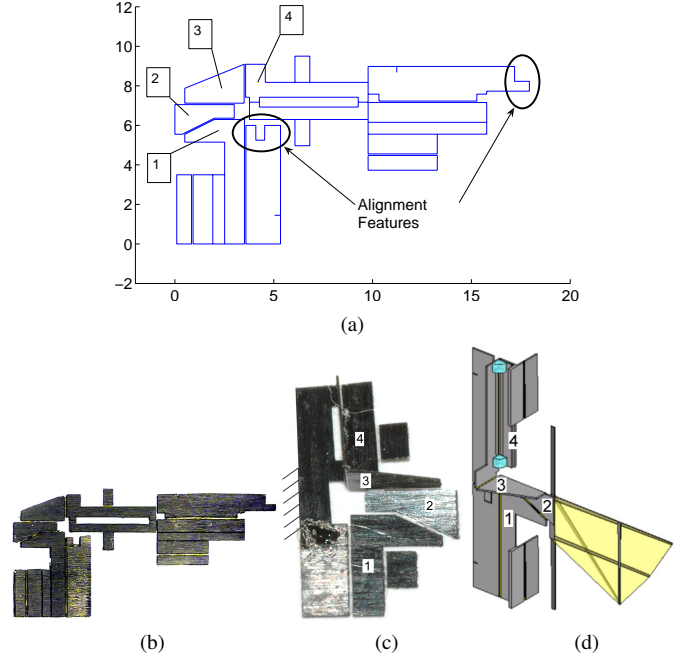

Fig. 7.   Example cut file with alignment features (a). Upon successful completion of this 2D laminate (b), these tabs are mated together to ensure proper joint alignment for the complete spherical five-bar differential (c). This differential is illustrated in (d) for use in a wing transmission mechanism.

where k_n^{link} and k_i are the link and flexure stiffnesses, respectively, $[D]$ is the reduced stiffness for bending moments (equivalent to EI/b) that will be defined later, and b_n is the width of the nth link. Therefore, for the ensuing energy calculations, the links are treated as rigid bodies.

A. Mass and inertia calculations

The link mass is given as follows:

$$m_i = l_i b_i \sum_k \rho_k \left(z_k - z_{k-1}\right) \tag{8}$$

where ρ_k is the density of the kth lamina and z_k is the directed height of the kth lamina with respect to the mid plane as is shown in Fig. 9(b). To calculate the effective inertia for an open or closed chain, we would first calculate the total kinetic energy (KE). This will in general be a function of the position and velocity of the center of gravity (CG) of each link as well as the angular velocity of each link about its CG. For an N-link chain, this is given as follows:

$$KE = \sum_{i=1}^{N} \left[\frac{1}{2} m_i v_{cg,i}^T v_{cg,i} + \frac{1}{2} \omega_i^T \mathcal{I}_i \omega_i \right] \tag{9}$$

where $\mathcal{I}_i$ is the inertia tensor of the ith link in the inertial reference frame, $v_{cg,i}$ and ω_i are the linear and angular velocities (about the center of gravity) of the ith link respectively. The velocity terms can be calculated from the Jacobians as follows [16]:

$$v_{cg,i} = J_{v_i}\left(q\right)\dot{q}, \qquad \omega_i = J_{\omega_i}\left(q\right)\dot{q} \tag{10}$$

where the q terms are the generalized coordinates (in this case the joint angles), and J_{v_i} and J_{ω_i} are the Jacobian matrices for the ith link corresponding to translation and rotation respectively. Now the kinetic energy can be rewritten as follows:

$$KE = \frac{1}{2} \dot{q}^T I\left(q\right) \dot{q} \tag{11}$$

where $I(q)$ is the system's inertia matrix,

$$I(q) = \left[\sum_{i=1}^{N} \left(m_i J_{v_i}(q)^T J_{v_i}(q) + J_{\omega_i}(q)^T \mathcal{I}_i J_{\omega_i}(q) \right) \right] \quad (12)$$

The derivation of the Jacobian is historically well established and outside the scope of this paper, however, as an example, consider a closed-chain single input, single output system (a four-bar linkage) as is shown in Fig. 8(a). The generalized coordinate for this system is the joint angle α with the 'output' for this system being the angle β. Thus for $L_1 > L_3$, this system amplifies angular motions as is shown in Fig. 8(b). Analytically solving for the kinematics and Jacobian is cumbersome, however, numerical simulation using equ. (12) can easily give the inertia properties for the four-bar as a function of the input and the link mass from equ. (8).
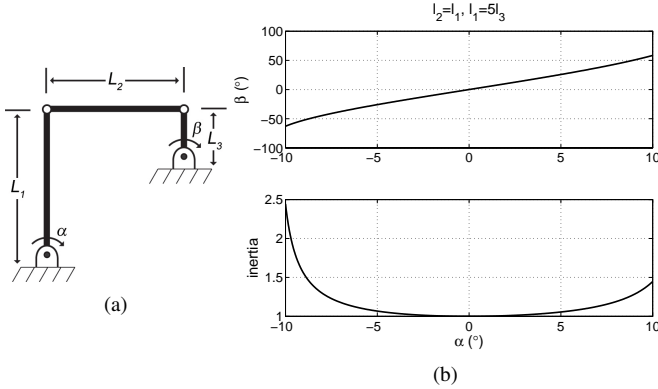

(a)

(b)

Fig. 8. Closed-chain four-bar schematic (a) and typical input-output characteristics and normalized inertia (b).

B. Laminate plate theory

Since each structural element created with SCM is a laminated beam comprised of flat plates, and each plate is assumed to have a thickness much less than either its width or length, a plane stress state can be assumed in which z-axis stresses are ignored. This allows us to analyze the system using a reduced tensor notation called laminate plate theory. This gives versatility to analytical or numerical analysis of such systems and includes all deformations of a beam in response to internal or external forces and moments. To begin the analysis, individual ply stresses and strains are defined as follows:

$$\begin{bmatrix} \sigma_x \\ \sigma_y \\ \tau_{xy} \end{bmatrix}_k = \begin{bmatrix} \overline{Q_{11}} & \overline{Q_{12}} & \overline{Q_{16}} \\ \overline{Q_{12}} & \overline{Q_{22}} & \overline{Q_{26}} \\ \overline{Q_{16}} & \overline{Q_{26}} & \overline{Q_{66}} \end{bmatrix}_k \begin{bmatrix} \epsilon_x \\ \epsilon_y \\ \gamma_{xy} \end{bmatrix}_k \quad (13)$$

Where $[\overline{Q_{ij}}]_k$ is the adjusted stiffness matrix whose elements have the following properties:

$$[\overline{Q_{ij}}]_k = [T]_k^{-1} [Q_{ij}]_k [T]_k^{-T} \quad (14)$$

and the matrix $[T]_k$ is the rotational matrix for the kth lamina with orientation θ_k as shown in Fig. 9(a):

$$[T]_k = \begin{bmatrix} m^2 & n^2 & 2mn \\ n^2 & m^2 & -2mn \\ -mn & mn & m^2 - n^2 \end{bmatrix}_k \quad (15)$$

where $m = \cos\theta_k$ and $n = \sin\theta_k$.

Now the forces and moments (per unit width) are calculated by integrating the stress over the thickness:

$$\begin{aligned} [N] &= \sum_k \int_{z_{k-1}}^{z_k} [\sigma_i]_k \ dz \\ [M] &= \sum_k \int_{z_{k-1}}^{z_k} [\sigma_i]_k z \ dz \end{aligned} \quad (16)$$
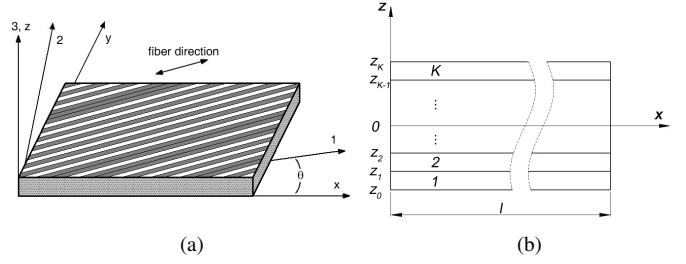

Fig. 9. Local and global lamina orientation description (a) and laminate geometric description (b).

Simplifying this notation by combining equ. (13) and (16) gives the relationship between the mid-plane strains and curvatures and the forces and moments:

$$\begin{bmatrix} N \\ M \end{bmatrix} = \begin{bmatrix} A_{ij} & B_{ij} \\ B_{ij} & D_{ij} \end{bmatrix} \begin{bmatrix} \epsilon^0 \\ \kappa \end{bmatrix} \quad (17)$$

The matrix containing the A, B, and D terms is called the stiffness matrix with elements defined as follows:

$$\begin{aligned} A_{ij} &= \sum_k [\overline{Q_{ij}}]_k (z_k - z_{k-1}) \\ B_{ij} &= \tfrac{1}{2} \sum_k [\overline{Q_{ij}}]_k (z_k^2 - z_{k-1}^2) \\ D_{ij} &= \tfrac{1}{3} \sum_k [\overline{Q_{ij}}]_k (z_k^3 - z_{k-1}^3) \end{aligned} \quad (18)$$

C. Integration of Active Laminae

In equ. (17), the total forces and moments per unit width $[N\ M]^T$ can be split up into discrete terms representing the contributions of various active laminae. For example, external (external loads) and internal (e.g. piezoelectric layers or coefficient of thermal expansion (CTE) mismatches) forces and moments per unit width are represented as follows:

$$\begin{bmatrix} N^{\text{tot}} \\ M^{\text{tot}} \end{bmatrix} = \begin{bmatrix} N^{\text{ext}} \\ M^{\text{ext}} \end{bmatrix} + \begin{bmatrix} N^p \\ M^p \end{bmatrix} + \begin{bmatrix} N^t \\ M^t \end{bmatrix} \quad (19)$$

Solving equ. (17) for the mid-plane strains and curvatures yields the following:

$$\begin{bmatrix} \epsilon^0 \\ \kappa \end{bmatrix} = \begin{bmatrix} A_{ij} & B_{ij} \\ B_{ij} & D_{ij} \end{bmatrix}^{-1} \begin{bmatrix} N^{\text{tot}} \\ M^{\text{tot}} \end{bmatrix} \quad (20)$$

The inverted stiffness matrix is the compliance matrix, $[C]$.

Proposition 1: *The compliance matrix exists and $[\epsilon^0 \kappa]^T$ is unique.* This is shown by construction in the Appendix.

The piezoelectric forces and moments are defined as follows:

$$\begin{aligned} [N_i]^p &= \sum_k \int_{z_{k-1}}^{z_k} [\overline{Q_{ij}}]_k d_{3j} E_3 \ dz \\ [M_i]^p &= \sum_k \int_{z_{k-1}}^{z_k} [\overline{Q_{ij}}]_k d_{3j} E_3 z \ dz \end{aligned} \quad (21)$$

where the d_{3j} and E_3 terms are the piezoelectric coupling coefficients and the electric field through the thickness of the lamina respectively. Similarly, thermal expansion forces and moments are:

$$\begin{aligned} [N_i]^t &= \sum_k \int_{z_{k-1}}^{z_k} [\overline{Q_{ij}}]_k [\overline{\alpha_j}]_k \Delta T \ dz \\ [M_i]^t &= \sum_k \int_{z_{k-1}}^{z_k} [\overline{Q_{ij}}]_k [\overline{\alpha_j}]_k \Delta T z \ dz \end{aligned} \quad (22)$$

where ΔT is the temperature change and the transformed CTE terms $[\overline{\alpha_i}]$ are as follows:

$$[\overline{\alpha}]_k = [T]_k^{-1} [\alpha]_k \quad (23)$$

The deformation of the beam is now fully defined by the mid-plane strain and curvature terms in (20).

Thus if some of the laminate materials are piezoelectric, the application of an electric field will produce a stress according to (21).

Similarly, if there is a mismatch between lamina CTEs, thermal forces and moments are obtained by adjusting the laminate temperature. These are two specific examples, however lamina with other modes of actuation are also encompassed within the model such as: shape memory alloys, electrostrictive materials, electroactive polymers, magnetostrictive materials, etc. Any material which changes its geometry (in a simple manner) in response to an applied excitation (magnetic field, electric field, current, temperature change, etc) can be used so long as it is a thin lamina. As a caveat to this, the active lamina need not be amorphous. For example, bundles of piezoelectric fibers would not be modeled using this method. However, binding these fibers within a matrix and creating a thin piezoelectric composite lamina, then assuming the beam is amorphous (with properties estimated from a rule of mixtures) is also encompassed[7].

For many of the materials mentioned, force transduction can be invertible. Some of the same materials that can be used to create actuators can also be used to sense loads applied to the structure.

D. Integration of Compliant Conductors

For the majority of transducers considered here, electric signals need to be brought to or from the links. Since all the cases here describe systems which have meticulously designed dynamic properties, stringing discrete wires in parallel with the flexures is out of the question, particularly when crossing joints undergoing large angular motions. Proximal actuation is a key benefit to parallel mechanisms. However, distally located sensors and/or actuators are often necessary or highly desirable and thus the problem of electrical connections over joints needs to be addressed.

There are two considerations to address for this problem. First, the wiring across the joint must remain intact over a large range of motion yet not interfere with the operation of the joint. Second, the wiring needs to facilitate electrical connections to the rest of the structure in an easy and reliable manner. Ideally, we would like the wiring to be directly integrated into the flexure joint. However, directly printed wires on the joint are prone to cracking and potentially add undesirable stiffness. With this in mind, we chose to keep the wiring as a separate ribbon structure looped over the joint (see Fig. 10). Although this wiring will form a large loop, its mechanical parameters can be calculated by using beam flexure formulas discussed previously (since the thickness of the ribbon is very small compared to the radius of the loop [17]). Also, because the ribbon cable wiring is parallel to the flexure joint, the total stiffness of the joint is the sum of the stiffnesses of the ribbon and the flexure. Given the material properties of the wiring, this ribbon loop can be designed to have negligible impact on the stiffness of the joint.

For the material of the wiring, we chose a metal foil (either copper or gold, $\approx 5\mu$m thick) with emphasis on integrity and reliability. The foil is patterned into discrete wires (400μm wide wires with 150μm spacing) using the SCM process. An adhesion promoter is then spin-coated onto the patterned foil, and polyimide[8] is spin-coated on top of the foil (to be used as an adhesion layer). To form a suitable substrate, polyimide (Kapton) is soft-baked on a hot plate at approximately $100°$C for 10-20 minutes. The wire ribbon (patterned foil and Kapton substrate) is then released and hard baked separately for an additional 20 to 30 minutes at over $300°$C to remove any remaining solvents. This ribbon can now be laser micromachined and used as any other layer in the SCM process.

To facilitate electrical interconnections, the ends of these wires are tinned with a low melting point solder. Two wires can be connected
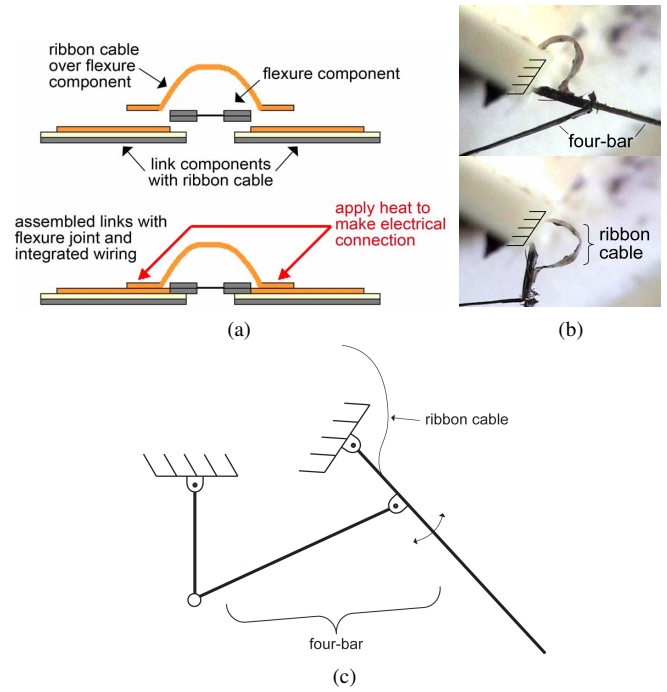

Fig. 10. Components and assembly method to integrate wiring over the flexure joints (a). In (b), a complete ribbon cable is integrated with a four-bar mechanism (illustrated in (c)) and actuated through a large displacement ($\approx 90°$) as a proof-of-concept.

together by layering the solder-coated sides together and a quick application of heat. (Again, see Fig. 10(a)).

It should be noted that other materials, such as conductive polymers, could also be implemented as a wiring material as long as the wiring loop across the joint is of sufficient length to keep the conductors intact and the stiffness of the loop low (i.e., $<<$ than the stiffness of the joint).

V. RESULTS

A. Articulated microstructures

The paradigm that has been described here gives the user the capability to create a broad array of articulated structures. Examples include a slider-crank, four-bar, five-bar, and Sarrus linkage. These are only a small subset of the devices that can be constructed. The only limitation of the SCM process is revolute joints; any articulated structure can be created using this process so long as the joints rotate through less than 2π (although $\pm\pi/3$ is a more practical limit). As a first example of a complex articulated microstructure, Fig. 11 shows a transmission system consisting of two slider-cranks, two parallel four-bars, and a spherical five-bar differential. The five-bar portion of the structure in Fig. 11 is displayed in greater detail in Fig. 5 and Fig. 7 and a four-bar design is illustrated in Fig. 6(c) and Fig. 8(a).

In some cases it is desirable to couple linear motion. In such cases, a Sarrus linkage can be used [18]. This is an additional microstructure enabled by this process and is illustrated in Fig. 12.

B. SCM actuators

As was described in sec. IV-C, incorporating electroactive laminae can produce induced-strain actuators. Using the analysis presented earlier, a geometric configuration was determined for optimal power transduction for a target microrobotic structure (in this case, the wing transmission of a flying robotic insect). The actuators depicted in Fig. 13 are 10mm long, have up to $\pm250\mu$m displacement, can provide ±50mN of force, and weigh $\approx$10mg each [9]. At an operating

---

[7]this is exactly analogous to the assumptions made for fiber-reinforced composite materials in general

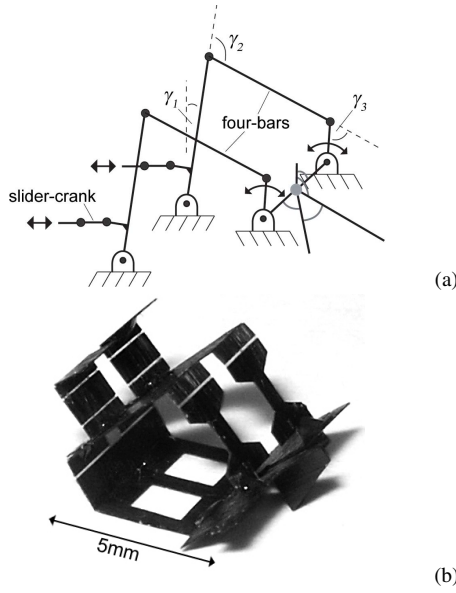[8]PI2525 or PI2611 from HD Microsystems

Fig. 11. Example 2DOF transmission system containing 15 joints (a). This is shown along side a SCM instantiation (b).
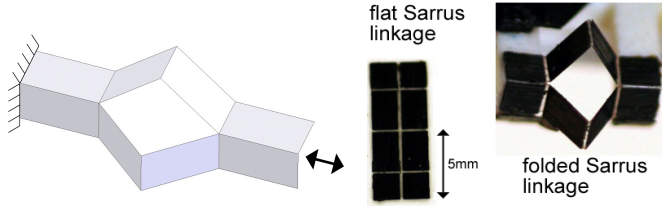

Fig. 12. Sarrus linkage used as a linear translational bearing.

frequency of 200Hz (quasi-static), these actuators can produce power densities $>300\mathrm{Wkg}^{-1}$ which is comparable to high performance DC motors.
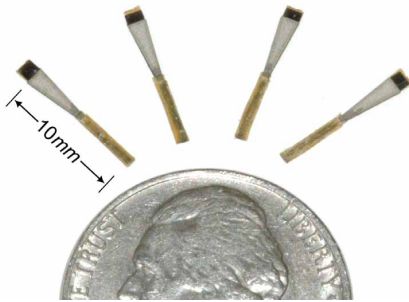

Fig. 13. Composite bimorph PZT-based actuators to be used as clamped-free bending cantilevers.

C. Rigid Microstructures

Using the principle of tensegrity [19] and the process described here for articulated joints, extremely rigid microstructures can be created. Links and joints are constructed using SCM and the joints are folded out of plane and frozen to create closed-chain three dimensional structures. If the ratio of links to joints satisfies Maxwell's rule ($n_l > 3n_j - 6$, where n_l and n_j are the number of links and joints in the structure respectively), the resulting structure is impervious to loads many orders of magnitude greater than its mass as is shown in Fig. 14(a). Note that this morphology requires links which are

extremely stiff in tension. This is a further merit of fiber-reinforced composite materials for this application.
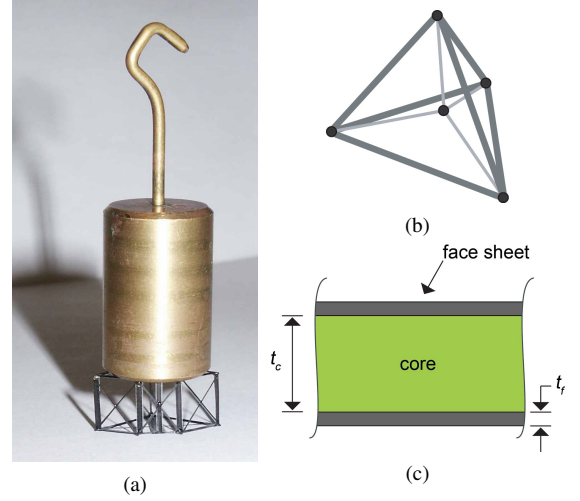

Fig. 14. Example of a rigid microstructure: a microrobot exoskeleton (a). Here a 20g mass is applied to a 20mg structure with no observable deformation. For a clearer illustration of a tensegrity structure, (b) shows a configuration of 10 links and 5 joints: since $10 > 3 \times 5 - 6$, this structure is considered rigid. Also, (c) shows a honeycomb-core-based laminate for rigid microstructures.

To quantify the benefit of utilizing tensegrity, a FEA model of the microrobot exoskeleton shown in Fig. 14(a) was created and loaded along the three principle cartesian axes. The normalized numerically estimated stiffnesses are shown in Fig. 15.
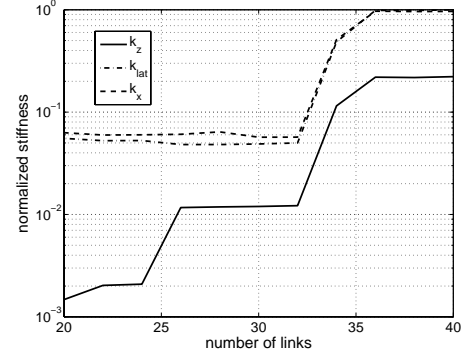

Fig. 15. Normalized stiffnesses as a function of the number of links applied to an example tensegrity structure. Note that in this case, the stiffness dramatically increases at 34 links. k_z, k_{lat}, and k_x are the normalized stiffnesses in the z (top-to-bottom), lateral (side-to-side), and x (front-to-back) directions of the structure in Fig. 14(a) respectively.

Alternatively, for known bending loads, extremely rigid structures can be created using the traditional honey-comb method. The reduced stiffness of the structure shown in Fig. 14(c) is approximated by the following (for $t_c >> t_f$):

$$EI_{hc} = \frac{t_f t_c^2 w}{2} E_f \qquad (24)$$

Thus the ratio of stiffness for this link to one without a core is $\propto t_c^2 / t_f^2$. If the core can be sufficiently lightweight (core density $<<$ face sheet density), this can be used to increase the strength-to-weight ratio (for bending moments). While it is difficult to manufacture a traditional honeycomb core at this scale, there are extremely lightweight polymers that can be used such as Aerogel[9]

[9]www.aerogel.com

($\rho = 130\text{kg·m}^{-3}$). Manufacturing such materials is feasible with the high aspect ratio (>10) laser micromachining system used in SCM.

D. Integrated sensors and compliant conductors

The wiring scheme was successfully tested by using it to wire a distally located strain gage across a four-bar leg joint undergoing large angular motions (over $75°$, see Fig. 10(b)). The wiring remained intact, had negligible impact on the motion of the joint, and we were able to successfully measure contact forces of the leg impacting a structure while it underwent this motion. Fig. 16 shows example results from a microrobot leg contacting a surface.
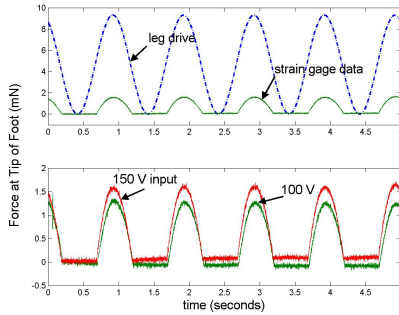

Fig. 16. Example results of incorporating strain sensors to measure contact forces in a microrobotic leg structure.

VI. COMPLETE SYSTEMS

A. Flapping-Wing Micro Air Vehicle Thorax

The Micromechanical Flying Insect (MFI) project began with the goal of creating a robotic insect capable of sustained autonomous flight [20]. Biological inspiration was used to limit the design space of the wing transmission system. However, there was still a significant challenge to recreating complex wing motions for a 1cm long airfoil. This was a challenge that could not be met using MEMS processes or any existing 'macro'-mechanical manufacturing techniques (for example Shape Deposition Manufacturing [21]). Instead, a transmission based upon impedance matching parallel mechanisms was created using slider-cranks, four-bars, and a spherical five-bar differential (collectively called the thorax as shown in Fig. 11). Combined with actuators and a tensegrity exoskeleton, this resulted in a two-wing, 4DOF microrobotic structure weighing 120mg that can recreate insect wing motions as is shown in Fig. 17.
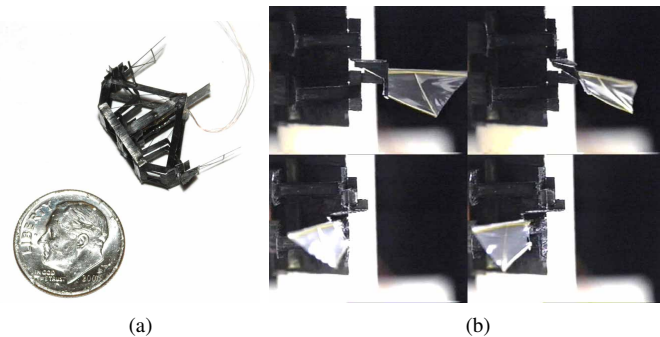

Fig. 17. Example microrobotic structure: (a) the Micromechanical Flying Insect and (b) a sample wing motion (wing beat frequency is 200Hz).

B. Crawling Microrobot Transmission

Ambulatory locomotion is another appropriate application for the structures created with SCM. To create a crawling mechanism, a slider-crank was chosen to form each leg where the crank was extended to become the leg and the slider was connected to the side driven by the actuator. For static and dynamic stability, a six-legged mechanism was chosen. To simplify the device (to use only two actuators), the motion of three of the legs (front and back of one side and the center of the other) were tied together by connecting the sliders to a common plate. Actuating the two plates $180°$ out of phase with each other will result in a tripod gait similar to that seen in nature. Linear motion of the plates was achieved through the use of Sarrus linkages that attach each plate to the base structure in three places.

Because the slider-crank has only one degree of freedom, the foot of the mechanism never gets truly picked off the ground. To overcome this deficiency, an additional flexure is included in the leg that has a mechanical stop on one side. This permits the leg to flex as it is dragged in one direction while being rigid in the opposite direction creating an asymmetry in force that results in forward motion of the mechanism. The analysis of the leg mechanism from actuator to ground reduces to the study of three sequential slider-crank mechanisms. The resulting structure was fit to a molded polymer endoskeleton and driven with SCM piezoelectric actuators. Further, on-board electronics were incorporated for sensing, communication, control, and power electronics (similar to the board created in [22]). Details of this analysis can be found in [23].
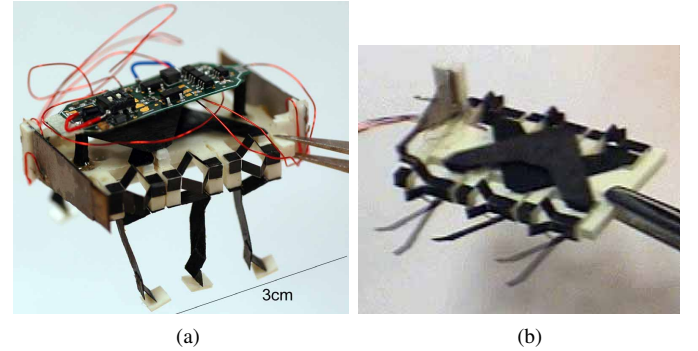

Fig. 18. Example microrobotic structure: crawling robotic insect (a) and sample leg motion (composite from a video sequence) (b).

VII. DISCUSSION

As stated, 'macro'-scale design methodologies are inappropriate to meet the demands of robust, high-performance micromechanical structures. The Smart Composite Microstructures process is detailed here as an enabling paradigm for such structures and numerous examples are given for the design of micromechanical components and integrated systems. The fundamental contributions of this work can be summarized as follows:

- We offer a complete fabrication solution for actuators, links, flexures, integrated wiring, and structural (ground) elements using high performance materials
- We describe simple design rules for flexures, links, and rigid structural elements
- Finally, we present combined working articulated microstructures with integrated piezoelectric actuators, wiring, and sensors. We also present two entire robotics structures utilizing the entire process and components

In this paper, we describe the SCM process as a paradigm that incorporates all the mechanical and electromechanical devices that are

required for the creation of complete, high performance microrobotic structures. This is something that has not been addressed or attempted elsewhere (either at this scale or with this complexity).

One aspect of the SCM process that is not obvious is the ease with which it is utilized. For example, the MFI structure shown in Fig. 17 was constructed in days with the vast majority of that time allocated to laser cutting and laminate curing. There are minimal barriers to implementing this process, both in terms of the infrastructural cost and the instruction necessary to understand the process steps. The performance of the resulting structures is largely dependent upon the materials used. For example, Kapton flexures can experimentally survive over one million cycles of large angle deflections. However, this may be significantly reduced for a less appropriate choice of flexure material.

REFERENCES

[1] W.S.N. Trimmer. Microrobots and micromechanical systems. *J. of Sensors and Actuators*, 19:267–287, 1989.

[2] K.S.J. Pister, M.W. Judy, S.R. Burgett, and R.S. Fearing. Microfabricated hinges. *J. of Sensors and Actuators A: Physical*, 33:249–256, 1992.

[3] R. Yeh, E.J.J. Kruglick, and K.S.J. Pister. Surface-micromachined components for articulated microrobots. *J. of Microelectrical Mechanical Systems*, 5(1):10–17, March 1996.

[4] R. Yeh, S. Hollar, and K.S.J. Pister. Design of low-power silicon articulated microrobots. *J. of Micromechatronics*, 1(3):191–203, 2002.

[5] S. Hollar, A. Flynn, C. Bellew, and K.S.J. Pister. Solar powered $10mg$ silicon robot. In *MEMS*, Kyoto, Japan, January 2003.

[6] T. Ebefors, J.U. Mattsson, E. Kälvesten, and G. Stemme. A walking silicon micro-robot. In *The 10th Int. Conf. on Solid-State Sensors and Actuators (Transducers '99)*, pages 1202–1205, Sendai, Japan, June 1999.

[7] R.J. Wood, S. Avadhanula, M. Menon, and R.S. Fearing. Microrobotics using composite materials: The micromechanical flying insect thorax. In *IEEE Int. Conf. on Robotics and Automation*, Taipei, Taiwan, September 2003.

[8] R.J. Wood, E. Steltz, and R.S. Fearing. Nonlinear performance limits for high energy density piezoelectric bending actuators. In *IEEE Int. Conf. on Robotics and Automation*, Barcelona, Spain, April 2005.

[9] R.J. Wood, E. Steltz, and R.S. Fearing. Optimal energy density piezoelectric bending actuators. *J. of Sensors and Actuators A: Physical*, 119(2):476–488, 2005.

[10] L. L. Howell. *Compliant mechanisms*. John Wiley and Sons, Inc., 2001.

[11] M. Goldfarb and J.E. Speich. A well-behaved revolute flexure joint for compliant mechanism design. *J. of Mechanical Design*, 121:424–429, September 1999.

[12] S. Avadhanula and R.S. Fearing. Flexure design rules for carbon fiber microrobotic mechanisms. In *IEEE Int. Conf. on Robotics and Automation*, Barcelona, Spain, April 2005.

[13] Y.-M. Moon, B.P. Trease, and S. Kota. Design of large-displacement compliant joints. In *Proc. of DETC'02: MECH 27th Biennial Mechanisms and Robotics Conference*, Montreal, Canada, October 2002.

[14] B.P. Trease, Y.-M. Moon, and S. Kota. Design of large-displacement compliant joints. *J. of Mech. Design*, 127:788–798, July 2005.

[15] A.E. Guérinot, S.P. Magleby, L.L. Howell, and R.H. Todd. Compliant joint design principles for high compressive load situations. *J. of Mech. Design*, 127:774–781, July 2005.

[16] M.W. Spong, S. Hutchinson, and M. Vidyasagar. *Robot Modeling and Control*. Wiley, 2006.

[17] R. B. Hopkins. *Design analysis of shafts and beams*. McGraw Hill, 1970.

[18] H.D. Eckhardt. *Kinematic Design of Machines and Mechanisms*. McGraw-Hill Professional, 1998.

[19] C.R. Calladine. Buckminster Fuller's "tensegrity" structures and Clerk Maxwell's rules for the construction of stiff frames. *Int. J. Solids Structures*, 14:161–172, 1978.

[20] R.S. Fearing, K.H. Chang, M. Dickinson, D.L. Pick, M. Sitti, and J. Yan. Wing transmission for a micromechanical flying insect. In *IEEE Int. Conf. on Robotics and Automation*, April 2000.

[21] S.A. Bailey, J.G. Cham, M.R. Cutkosky, and R.J. Full. Biomimetic robotic mechanisms via shape deposition manufacturing. In 9th *Intl. Symp. of Robotics Research*, pages 321–327, Snowbird, Utah, October 1999.

[22] R.J. Wood, S. Avadhanula, E. Steltz, M. Seeman, J. Entwistle, A. Bachrach, G. Barrows, S. Sanders, and R.S. Fearing. Design, fabrication and initial results of a 2g autonomous glider. In *Conf. of IEEE Industrial Electronics Society*, Raleigh, NC, November 2005.

[23] R. Sahai, S. Avadhanula, R. Groff, E. Steltz, R. J. Wood, and R. S. Fearing. Towards a 3g crawling robot through the integration of microrobot technologies. In *IEEE Int. Conf. on Robotics and Automation*, Orlando, FL, May 2006.

APPENDIX: PROOF OF PROPOSITION 1

For the compliance matrix to exist, the stiffness matrix must have full rank (i.e. rank 6). To show that this is always the case, consider the construction of the stiffness matrix:

$$\left[\begin{array}{c} N \\ M \end{array} \right] = \left[\begin{array}{cc} A & B \\ B & D \end{array} \right] \left[\begin{array}{c} \epsilon^0 \\ \kappa \end{array} \right] \tag{25}$$

Solving this for ϵ^0 gives:

$$\epsilon^0 = A^{-1}N - A^{-1}B\kappa \tag{26}$$

Including this in (25) and rearranging gives:

$$\left[\begin{array}{c} \epsilon^0 \\ M \end{array} \right] = \left[\begin{array}{cc} A^{-1} & -A^{-1}B \\ BA^{-1} & D - BA^{-1}B \end{array} \right] \left[\begin{array}{c} N \\ \kappa \end{array} \right] \tag{27}$$

Similarly, solving (25) for κ gives:

$$\kappa = \left(D - BA^{-1}B\right)^{-1} M - \left(D - BA^{-1}B\right)^{-1} BA^{-1}N \tag{28}$$

Using this in (26) allows us to represent ϵ^0 in terms of N and M:

$$\epsilon^0 = \left(A^{-1} + A^{-1}B \left(D - BA^{-1}B\right)^{-1} BA^{-1}\right) N \\ - A^{-1}B \left(D - BA^{-1}B\right)^{-1} M \tag{29}$$

Arranging (28) and (29) in matrix form allows us to represent $[C]$:

$$\left[\begin{array}{c} \epsilon^0 \\ \kappa \end{array} \right] = \left[\begin{array}{cc} A^* & B^* \\ H^* & D^* \end{array} \right] \left[\begin{array}{c} N \\ M \end{array} \right] \tag{30}$$

where the A^*, B^*, H^*, and D^* terms are given as follows:

$$\begin{array}{l} A^* = A^{-1} + A^{-1}B \left(D - BA^{-1}B\right)^{-1} BA^{-1} \\ B^* = -A^{-1}B \left(D - BA^{-1}B\right)^{-1} \\ H^* = - \left(D - BA^{-1}B\right)^{-1} BA^{-1} \\ D^* = \left(D - BA^{-1}B\right)^{-1} \end{array} \tag{31}$$

Thus to show that $[C]$ exists, it is sufficient to show that A^{-1} and $\left(D - BA^{-1}B\right)^{-1}$ exist. As an aside, if $[C]$ does exist, then it must be symmetric (since the inverse of a symmetric matrix is itself symmetric) and thus $B^* = H^*$. To show that A^{-1} exists, we note the construction of the matrix from (18). It is easy to see that from equ. (14) for the matrix $\left[\bar{Q}\right]$ to have full rank, both the matrices $[T]$ and $[Q]$ also have to be full rank (since $rank\,(XY) = min\,(rank\,(X), rank\,(Y))$). By the physical basis of the $[Q]$ matrix, it is alway full rank for any material and anisotropy. Similarly, for any value of θ, the matrix $[T]$ is always full rank. Further, $\left[\bar{Q}\right]$ is positive definite. As a final step, note that $(z_k - z_{k-1}) > 0 \forall k$. Thus, A is an increasing linear combination of positive definite matrices of similar form and is thus itself positive definite and full rank. An identical argument can be made for D since $\left(z_k^3 - z_{k-1}^3\right) > 0 \forall k$. For laminates that are symmetric about the mid-plane, B is zero and thus this proof is complete. For asymmetric laminates, we need to show that subtracting $BA^{-1}B$ does not diminish the rank of D.

This is significantly more involved and outside the scope of this paper. However, consider as a 'worst-case' a laminate that is anti-symmetric (two identical layers oriented at 0 and 90 degrees respectively). In this case it is easy to see that:

$$B = \begin{bmatrix} B_{11} & 0 & 0 \\ 0 & -B_{11} & 0 \\ 0 & 0 & 0 \end{bmatrix} = \begin{bmatrix} 1 & 0 & 0 \\ 0 & -1 & 0 \\ 0 & 0 & 0 \end{bmatrix} \frac{1}{4} \frac{(F-1)}{(F+1)} A_{11} t \tag{32}$$

where t is the thickness of each layer and F is the ratio of anisotropy ($= E_2/E_1$). For a high performance composite material, we can approximate $F \approx 0$ and B becomes:

$$B = \begin{bmatrix} -1 & 0 & 0 \\ 0 & 1 & 0 \\ 0 & 0 & 0 \end{bmatrix} \frac{1}{4} A_{11} t \tag{33}$$

Similarly, D can be shown to have the following form:

$$D = \begin{bmatrix} A_{11} & A_{12} & 0 \\ A_{12} & A_{11} & 0 \\ 0 & 0 & A_{66} \end{bmatrix} \frac{t^2}{12} \tag{34}$$

Now $D - BA^{-1}B$ is given as follows:

$$\begin{bmatrix} \frac{A_{11}}{16}\left(\frac{1}{12} - \frac{A_{11}^2}{A_{11}^2 - A_{12}^2}\right) & \frac{A_{12}}{16}\left(\frac{1}{12} - \frac{A_{11}^2}{A_{11}^2 - A_{12}^2}\right) & 0 \\ \frac{A_{12}}{16}\left(\frac{1}{12} - \frac{A_{11}^2}{A_{11}^2 - A_{12}^2}\right) & \frac{A_{11}}{16}\left(\frac{1}{12} - \frac{A_{11}^2}{A_{11}^2 - A_{12}^2}\right) & 0 \\ 0 & 0 & \frac{A_{66}}{12} \end{bmatrix} t^2 \tag{35}$$

For this to be singular, either $A_{11} = A_{12}$ or $(A_{12}/A_{11})^2 = -11$. Neither of these conditions will ever be met for any physical composite.